

Resonance Effects in the Bent Waveguide-Based Fabry–Perot Resonator with Mirrors of Spatially Varying Reflectivity

A. V. Dyshlyuk^{a, b, c, *} and O. B. Vitrik^{a, b}

^a Institute of Automation and Control Processes, Far Eastern Branch, Russian Academy of Sciences, Vladivostok, 690041 Russia

^b Far Eastern Federal University, Vladivostok, 690091 Russia

^c Vladivostok State University of Economics and Service, Vladivostok, 690014 Russia

*e-mail: anton_dys@mail.ru

Received September 20, 2022; revised October 14, 2022; accepted October 20, 2022

Abstract—High- Q Fano resonances and effects like electromagnetically induced transparency have been demonstrated in the bent waveguide-based Fabry–Perot resonator with mirrors of nonuniform reflectivity. The phenomena are shown to arise from the coupling between the fundamental mode of the core and a whispering gallery mode of the bent waveguide’s cladding. The influence of all major geometric parameters of the resonator on the resonant features in its transmission and reflection spectra is investigated. The results obtained in the paper can find application in the design of novel functional elements of photonics, for example, portable high-resolution refractometers for bio- and chemosensing systems and optical sensors of mechanical effects such as strain, stress, deformation, or displacement.

Keywords: Fano resonance, electromagnetically induced transparency, bent waveguide, whispering gallery mode, optical sensor, optical refractometer, chemosensing, biosensing

DOI: 10.3103/S1062873822700381

INTRODUCTION

Fano resonances and related effects analogous to Autler-Townes splitting and electromagnetically induced transparency (EIT) [1–3] are attracting considerable attention of researchers in optics [2, 4–6], nanophotonics [2, 7–9], plasmonics [6, 10], quantum electronics [11], metamaterials [2, 6], optical chemo- and biosensing techniques [12–14], etc. The interest to such phenomena is since they provide flexible control over the spectral response of resonant systems, which makes it possible to tailor it to specific tasks and applications. For example, abrupt changes from maximum to near-zero values in transmission, absorption, scattering, or reflection spectra associated with high Q -factor Fano resonances and EIT-like regimes enable the design of sensing and switching photonic devices of very high resolution and selectivity [2, 6, 12–16].

In [17, 18] tunable Fano resonances and Autler-Townes-like splitting of resonances were demonstrated in a bent single-mode waveguide-based Fabry-Perot resonator (FPR) arising from the coupling between the fundamental mode (FM) of the core and whispering gallery mode (WGM) of the bent waveguide’s cladding. The discovered effects, however, have been shown to yield relatively smooth patterns in the transmission and reflection spectra of the resonator without particularly sharp features, which would be

promising for practical applications. It was suggested in [18], that such features may be obtained using mirrors of spatially varying reflectivity to provide a high Q -factor of the WGM-resonance and a low Q -factor of the FM-resonance. In this paper we show by the example of a simplified 2D geometry that the use of such mirrors does indeed lead to narrow-band Fano resonances and EIT-like features in the transmission and reflection spectra of the bent waveguide-based Fabry–Perot resonator. Given that they result from FM coupling with a cladding WGM, whose propagation constant depends on the bend radius and whose field evanescently penetrates into the medium surrounding the waveguide, the phenomena demonstrated in the paper open up exciting prospects of designing novel high-performance bent waveguide-based photonic devices such as, for example, portable refractometers for bio- and chemosensing applications as well as optical sensors of mechanical effects.

The paper is organized as follows. Firstly, we shall consider the coupling between the core mode and the cladding whispering gallery modes in a bent single-mode slab waveguide. Next, we shall show that because of the coupling a Fabry–Perot resonator formed by a section of such a waveguide with mirrors on its end faces works as a system of two coupled FM- and WGM-subresonators, with sharp symmetric and asymmetric resonance features appearing in its trans-

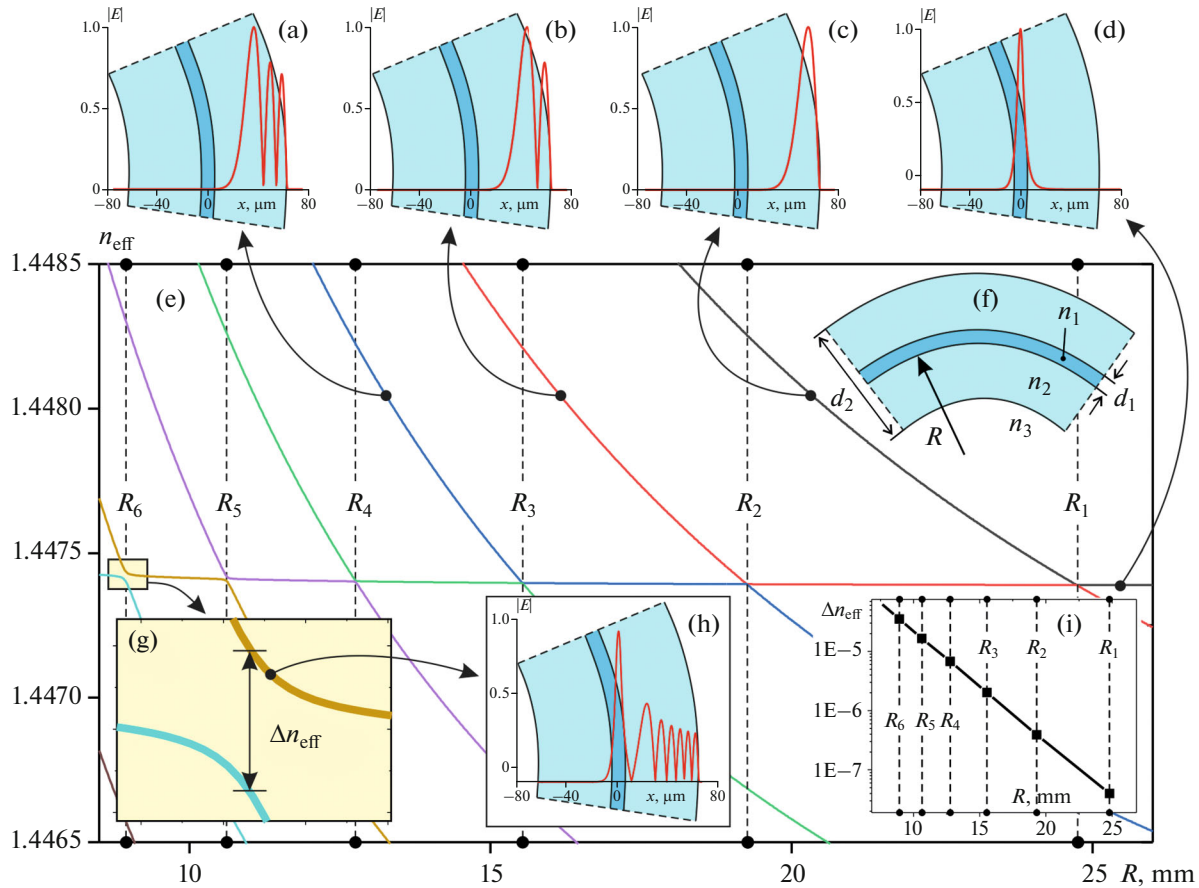


Fig. 1. Dependences of the effective refractive indices (n_{eff}) of MLBW modes on the bend radius (R) at a fixed wavelength of $\lambda = 1555$ nm (e). Insets: (a–d) amplitude profiles of MLBW modes calculated at non-resonant bend radii where they coincide with the profiles of WGMs (a–c) and FM (d) as viewed separately; (f) is a schematic view of the bent waveguide under study; (g) enlarged view of an anticrossing of the dispersion curves of the MLBW modes near the resonant bend radius R_6 ; (h) amplitude profile of one of the two MLBW modes at the resonant bend radius R_6 , resulting from hybridization of FM and WGM (the second mode’s profile looks similar and is not shown in the figure); (i) the amount of splitting of the dispersion curves of MLBW modes Δn_{eff} as a function of the resonant bend radius ($R_1 = 24.753$ mm, $R_2 = 19.269$ mm, $R_3 = 15.537$ mm, $R_4 = 12.764$ mm, $R_5 = 10.625$ mm, $R_6 = 8.932$ mm).

mission and reflection spectra that can be used for designing optical sensors of refractive index or mechanical effects. We shall then proceed to study the effect of all major geometric parameters of the bent FPR on the position, shape and sharpness of the resonance features in its spectra, establish what limits the latter parameter and how to achieve its highest values.

OBJECT AND METHODOLOGY OF THE STUDY

A schematic view of the bent slab waveguide is shown in Fig. 1f. Its parameters are chosen like those of a conventional single-mode optical fiber without a polymer coating, in air: $n_1 = 1.4504$, $d_1 = 4$ μm , $n_2 = 1.4447$, $d_2 = 125$ μm , $n_3 = 1$. Due to the total internal reflection at the interface between the cladding and the surrounding medium both the core and the cladding of the waveguide possess light-guiding properties.

To describe propagation of light along such a composite waveguide one can resort to two different approaches [20].

The first and more rigorous one consists in the decomposition of guided light into non-interacting modes of the entire multilayer bent waveguide (MLBW), considered as a whole. All the calculated results in this work were obtained by this method, using commercial software for numerical simulation of waveguiding devices Ansys Lumerical MODE.

In the second, approximate but more intuitive approach, the core and cladding of the bent waveguide are considered separately. The core guides a single fundamental mode, while the cladding supports multiple whispering gallery modes. The core and cladding modes in this approach can interact with each other: when the FM propagation constant match that of one of the WGMs, a strong coupling can arise between them, as described by the coupled mode theory [20].

We shall use this approach to interpret the numerical results.

In Fig. 1 we plot the effective indices of MLBW modes calculated as a function of the bend radius at a fixed wavelength of $\lambda = 1555$ nm. Both the effective indices and the profiles of MLBW modes (Figs. 1a–1d) mostly coincide with those of FM and WGM considered separately, except near certain resonant bend radii R_n (where n is the ordinal number of the resonance).

At those bend radii, where the effective indices of FM and WGM become equal, the dispersion curves of the MLBW modes exhibit characteristic anticrossing behavior [19] (Fig. 1g), while their profiles become hybridized and incorporate features of both FM and the corresponding WGM (Fig. 1h). This is a clear indication of the coupling between the fundamental mode of the core and the whispering gallery mode of the bent waveguide's cladding occurring at those bend radii where they become phase-matched.

In the waveguide theory, coupling between modes is usually classified into strong and weak, depending on whether the coupled modes have equal or different propagation constants [20]. In this work, however, since only resonant bend radii are of interest, where the effective indices of FM and WGM are practically the same, we shall characterize the strength of their coupling by the coupling coefficient. According to the coupled-mode theory, this coefficient is calculated through the overlap integral of the FM and WGM profiles [20], while in terms of MLBW modes it is proportional to the amount of splitting of their dispersion curves Δn_{eff} (Fig. 1f) at the corresponding anticrossing [19, 20]. The dependence of Δn_{eff} on the resonant value of the bend radius is shown in Fig. 1i. As can be seen, with increasing R_n , the value of Δn_{eff} and, consequently, the FM-WGM coupling strength decrease exponentially. It will be shown below that this circumstance turns out to be important for obtaining sharp resonant features in the reflection and transmission spectra of a Fabry–Perot resonator formed by a section of the bent waveguide with mirrors at its end faces.

A schematic view of such a bent waveguide resonator (BWR) is given in Fig. 2c. When a coupling occurs between the FM and WGM, the resonator can be considered as a system of two coupled FM- and WGM-subresonators, the first of which is excited by the radiation of the fundamental mode in the straight input Section 1, while the second receives energy through the coupling with the first. Radiation is output from the FM-subresonator through the straight output Section 5. As demonstrated in [17, 18], such an optical system is analogous to a mechanical system of two coupled pendulums P1 and P2 oscillating under the action of a harmonic driving force applied to one of them (Fig. 2d). If the pendulums have the same natural frequencies ($\omega_1 = \omega_2$) and the same damping ($\gamma_1 = \gamma_2$), then, in the strong coupling regime ($g \gg \gamma_1, \gamma_2$), split-

ting of the resonance lineshape is observed in the frequency response of the P1 pendulum, like the well-known Autler–Townes effect [19]. A similar splitting of resonance lines is observed in the reflection and transmission spectra of BWR with mirrors of uniform reflectivity furnishing equal radiative losses of the FM and WGM-subresonators, provided that their Q -factors are sufficiently large and FM-WGM coupling is sufficiently strong (i.e., bend radius is small enough) [17, 18].

Autler–Townes-like splitting of resonances resulting from the strong coupling of FM- and WGM-subresonators, however, does not lead to sharp variations and narrow-band resonant features in the BWR spectra, which would be attractive for practical applications. In the mechanical system of coupled pendulums, to obtain such features, for example, a sharp asymmetric Fano resonance or a narrow symmetric dip in a broad resonance lineshape characteristic of electromagnetically induced transparency, it is necessary, first, that the damping of pendulum P2 be significantly lower than that of pendulum P1 ($\gamma_2 \ll \gamma_1$); secondly, the coupling coefficient between them should be much smaller than the damping of the first pendulum ($g \ll \gamma_1$), which corresponds to the weak coupling regime [3]. For BWR under study, the conditions for obtaining narrow-band spectral features can be reformulated as follows: first, the Q -factor of the WGM-subresonator should be significantly higher than that of the FM-subresonator. Secondly, the FM-WGM coupling strength and the Q -factor of the FM-subresonator should be sufficiently low. These conditions can be easily satisfied by using nonuniform resonator mirrors, which provide a high reflectivity in the cladding a low reflectivity in the core region, combined with a sufficiently large resonant bend radius to guarantee the weak coupling regime of the FM and WGM-subresonators.

In this work, variable reflectivity mirrors are implemented in the simplest possible way by applying to the end faces of the bent waveguide section optically thick layers of silver (with dielectric permittivity $\epsilon_{\text{Ag}} \approx -130 + 3.3i$ at $\lambda \sim 1555$ nm [21]) with holes in the middle (Fig. 2c). The reflectivity of the mirror in the cladding region R_{clad} , calculated as a function of the silver layer thickness h_2 , is shown in Fig. 2e. As one can see, it rapidly increases with h_2 and at $h_2 \gtrsim 50$ nm it closely approaches 100%. The hole in the metal next to the waveguide core constitutes a weakly reflective interference mirror formed by the two endfaces of the waveguide with an air gap between them. Its reflectivity R_{core} calculated as a function of the gap thickness h_1 is also shown in Fig. 2e. It increases with h_1 much more slowly than R_{clad} , and even at $h_1 = 100$ nm reaches only about 2%. Thus, if we take $h_1 = h_2$ for simplicity, then with a thickness of such a composite mirror of several tens of nanometers, we have $R_{\text{clad}} \gg R_{\text{core}}$, which

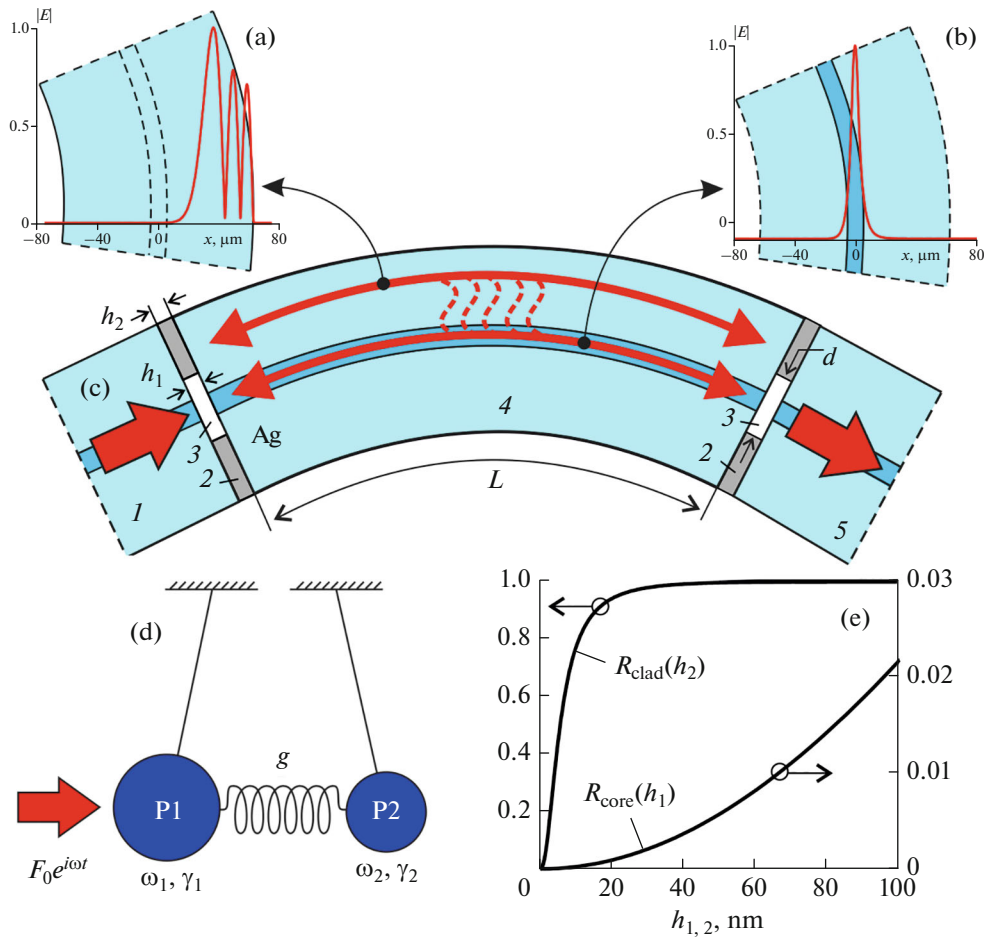


Fig. 2. Schematic view of the bent waveguide-based Fabry–Perot resonator with mirrors of nonuniform reflectivity consisting of silver layers with holes next to the waveguide core (c): (1) straight input waveguide section, (2) silver mirrors, (3) air gap near the waveguide core, (4) bent waveguide section, (5) straight output waveguide section. Insets: (a, b) amplitude profiles of FM and WGM, which couple together at $R \sim R_3 = 15.537$ mm, $\lambda = 1555$ nm; (d) mechanical analogy of the bent waveguide resonator consisting of two coupled pendulums oscillating under the action of a harmonic driving force applied to one of them; (e) calculated reflectivity of the air gap in the core region (R_{core}) and the silver layer in the cladding region (R_{clad}) vs. the corresponding thickness h_1 and h_2 .

ensures the fulfillment of the first of the above conditions, and, combined with the choice of a sufficiently large bend radius, allows one to expect sharp resonant features in the transmission and reflection spectra of the BWR.

RESULTS AND DISCUSSION

The transmission and reflection spectra of the bent waveguide resonator spectra calculated for four bend radii near $R_3 = 15.537$ mm are shown in Fig. 3. We see from Fig. 3a that, against the background of a weak sinusoidal modulation caused by the low-Q FM-subresonator, sharp, asymmetric Fano resonances do indeed appear in the spectra of the BWR. These narrowband resonances occur at the resonant wavelengths of the WGM-subresonator and are similar in shape to the Fano resonances in the frequency

response of the pendulum P1 in the analogous mechanical system. Note that such an asymmetric lineshape is an indication of unequal natural frequencies of the coupled pendulums [2]. This is also true for the coupled subresonators: as evident from Fig. 3a, the positions of the Fano resonances does not coincide with the maxima of the sinusoidal modulation in $T_{\text{FPR}}(\lambda)$, i.e., the resonant wavelengths of the FM and WGM-subresonators differ despite the fact that the propagation constants of the corresponding coupled modes coincide exactly at this bend radius. This is explained as follows. The resonant wavelengths of the FM and WGM-subresonators are dictated by the round-trip phase shift for the corresponding modes, including the phase shifts upon reflections from the mirrors, being a multiple of 2π . The phase shifts for light reflecting from the silver layer in the cladding and from the air gap in the core region are significantly

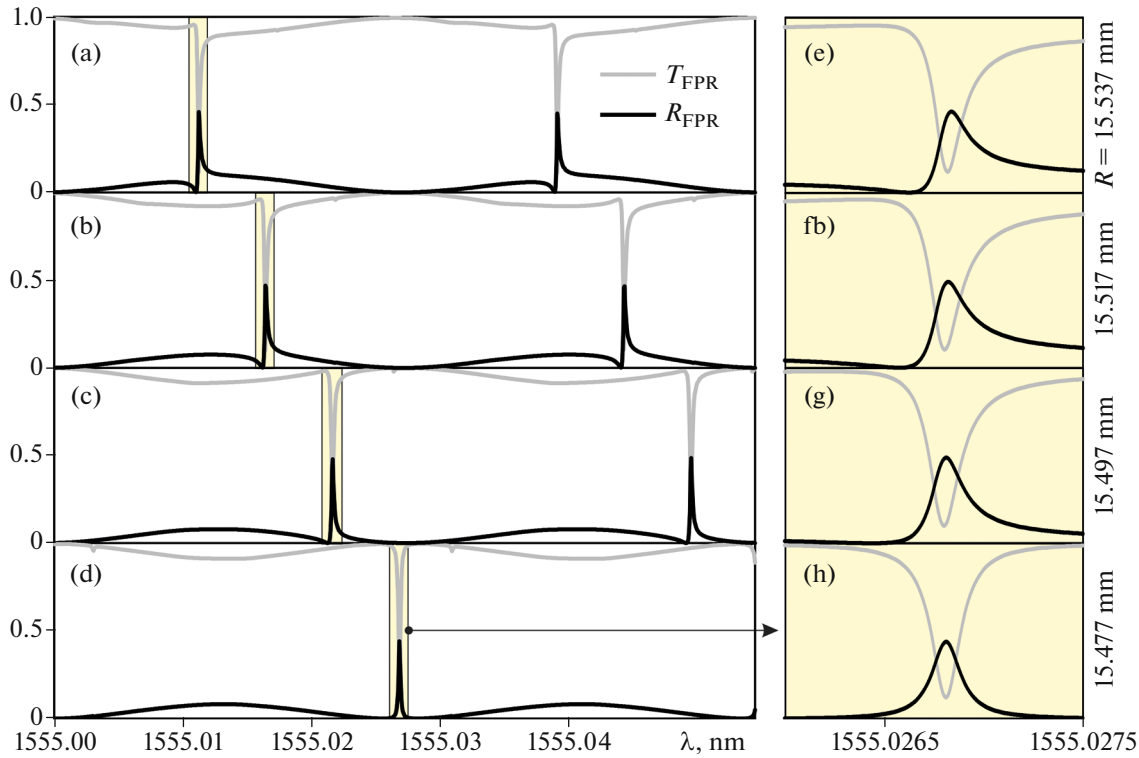


Fig. 3. Reflection $R_{\text{FPR}}(\lambda)$ and transmission $T_{\text{FPR}}(\lambda)$ spectra of the bent waveguide resonator ($R_{\text{FPR}}(\lambda) = P_{\text{R}}(\lambda)/P_0$, $T_{\text{FPR}}(\lambda) = P_{\text{T}}(\lambda)/P_0$, where P_0 is the power carried by the fundamental mode in the input Section 1 (Fig. 2c), $P_{\text{R}}(\lambda)$ is the power of the reflected FM in the same section, and $P_{\text{T}}(\lambda)$ is the power of the transmitted FM in the output Section 5, calculated at $R = 15.537$ mm (a, e), $R = 15.517$ mm (b, f), $R = 15.497$ mm (c, g) and $R = 15.477$ mm (d, h), $h_1 = h_2 = 100$ nm, $d = 30$ μm , $L = 30$ mm. The insets (e–h) are zoomed-in views of the resonant features.

different, which is what explains the difference in the resonant wavelengths of the FM and WGM-subresonators.

Note that due to the strong dependence of WGM's effective index on the waveguide curvature, the resonant wavelengths of the WGM-subresonator can be fine-tuned by slightly varying the bend radius near its resonant value. This, as illustrated in Figs. 3b, 3d, allows one to control the position and shape of the Fano resonances. At $R = 15.477$ mm (Figs. 3d, 3h) the resonances of the FM and WGM-subresonators are made to coincide, and the transmission spectrum of the BWR exhibits a narrow symmetrical dip in a broad resonance lineshape, which is characteristic of the electromagnetically induced transparency effect [2]. A similar dip occurs in the frequency response of the pendulum P1 in the mechanical oscillatory system at $\omega_1 = \omega_2$, $\gamma_2 \ll \gamma_1$ and $g \ll \gamma_1$ [3].

The strong dependence of the position of the Fano resonances on the bend radius can be utilized for designing high-precision sensors of mechanical effects affecting the curvature of the resonator. On the other hand, even at a constant bend radius the WGM effective index and, accordingly, the positions of the Fano resonances in the spectra of the BWR will depend on the ambient refractive index n_3 due to the WGM field

evanescently penetrating the external medium. This opens exciting prospects of building novel high-precision waveguide refractometers. In terms of their metrological performance, such sensors can surpass known bent waveguide-based refractometers [22–25] due to the sharpness of the demonstrated resonant features, which is one of the most important parameters defining the resolution of refractometric measurements [26].

In the context of the present work, the sharpness of a resonance lineshape (S) can be quantified by the ratio of its amplitude A (for example, the depth of the dip in the transmission spectrum) to its half-width W , normalized to the free spectral range of the resonator (FSR): $S = A \cdot \text{FSR} / W$ (see Figs. 4b and 4f). Reasoning from the mechanical analogy, we can expect S to depend primarily on the Q -factor of the WGM-subresonator, which is determined by its losses and length, and on the FM-WGM coupling strength, which is governed by the R_n value (Fig. 1f). We shall now illustrate the effect of these factors on the sharpness and shape of the Fano resonances in the BWR spectra.

The losses of the WGM-subresonator can be subdivided into radiative and dissipative. Radiation losses are caused by the WGM radiation escaping the reso-

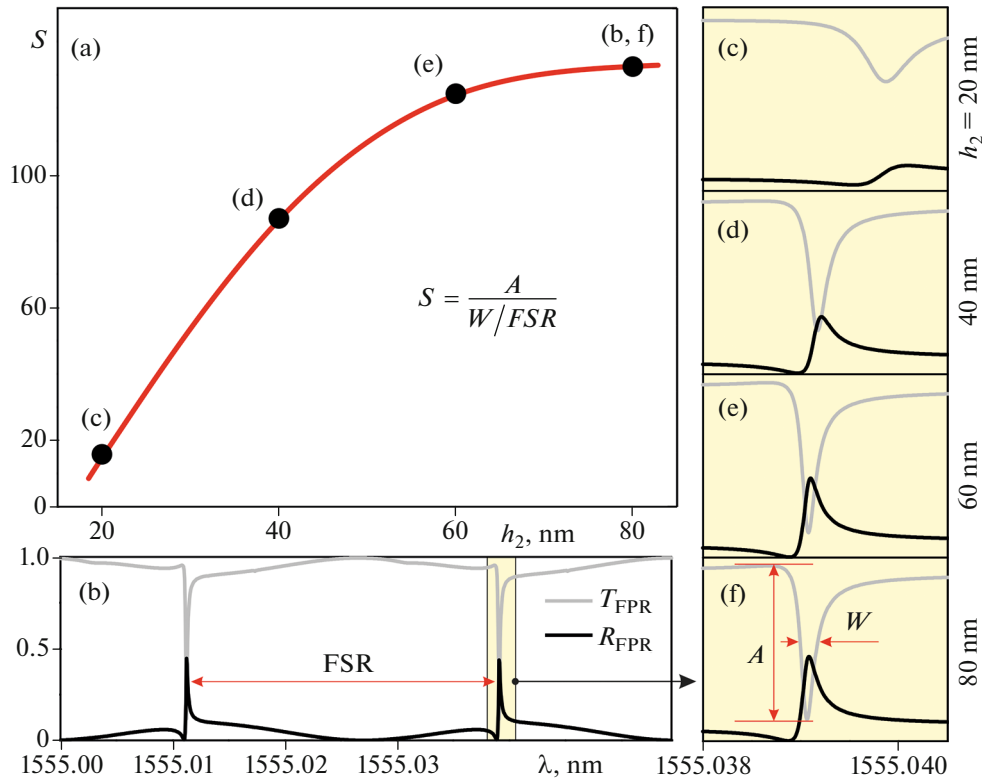


Fig. 4. Dependence of the sharpness S of the Fano resonance ($S = A \cdot FSR/W$, where $A = T_{\max} - T_{\min}$ is the difference between the maximum and minimum transmittance in the resonant dip, FSR is the free spectral range, W is the full width at the mean level of the dip $(T_{\max} + T_{\min})/2$) on the thickness of the metal mirrors (a); (b) Reflection (R_{FPR}) and transmission (T_{FPR}) spectra of the BWR calculated at $h_1 = 100$ nm, $h_2 = 80$ nm, $R = 15.537$ mm, $d = 30$ μ m, $L = 30$ mm. Insets (c–f) show zoomed-in views of the Fano resonance lineshape at $h_2 = 20$ nm (c), $h_2 = 40$ nm (d), $h_2 = 60$ nm (e), and $h_2 = 80$ nm (f).

nator due to the transmission through the metal mirrors, diffraction at the inner edges of the mirrors, and tunneling through the cladding surface into the external medium due to the waveguide bending [20]. However, for the bend radii considered in this work ($R > 10$ mm), the tunneling losses, as calculations show, turn out to be negligible, so the radiation losses of the WGM-subresonator are associated only with transmission through the mirrors and diffraction at their edges. Dissipative losses are also due to the mirrors and result from the absorption of light in silver due to the non-zero imaginary part of its dielectric permittivity. Note that absorption by the mirror is very small in the working spectral range: it is calculated to be only $\sim 0.65\%$ regardless of the mirror thickness h_2 for $h_2 \gtrsim 60$ nm. Nevertheless, at sufficiently low radiation losses, absorption will be shown below to become the dominant process limiting the Q -factor of the WGM-subresonator and to have a decisive effect on the shape and sharpness of the Fano resonances in the BWR spectra.

Let us first consider the role of the radiation losses of the WGM-subresonator associated with the transmission of light through the mirrors. The transmittance of metal mirrors, as evident from Fig. 2e, rapidly

decreases with mirror thickness h_2 , which means the sharpness of the Fano resonances should increase with h_2 due to the enhancement of the WGM-subresonator Q -factor. To confirm this, we plot in Fig. 4 the dependence $S(h_2)$, as well as the reflection and transmission spectra of the BWR calculated at $h_2 = 20, 40, 60,$ and 80 nm (for clarity, the transmission coefficient of the air gap in the core region, which determines the radiation losses of the FM-subresonator, was kept unchanged in the calculations due to the fixed thickness $h_1 = 100$ nm).

As can be seen from the figure, at small mirror thicknesses, the sharpness S does increase monotonically with h_2 , however, for $h_2 \gtrsim 60$ nm, the growth is saturated, and the spectra calculated at $h_2 = 60$ nm (Fig. 4e) and 80 nm (Fig. 4f) look the same. Note that the minimum in the resonance dip in the transmission spectrum does not reach zero even at $h_2 \gtrsim 60$. In the mechanical system of coupled pendulums (Fig. 2d), the fact that the resonance minimum in the frequency response of the pendulum P1 does not reach zero is an indication of non-zero damping of the pendulum P2. We can thus conclude that at $h_2 \gtrsim 60$ nm, the WGM-subresonator still has some non-zero losses, which,

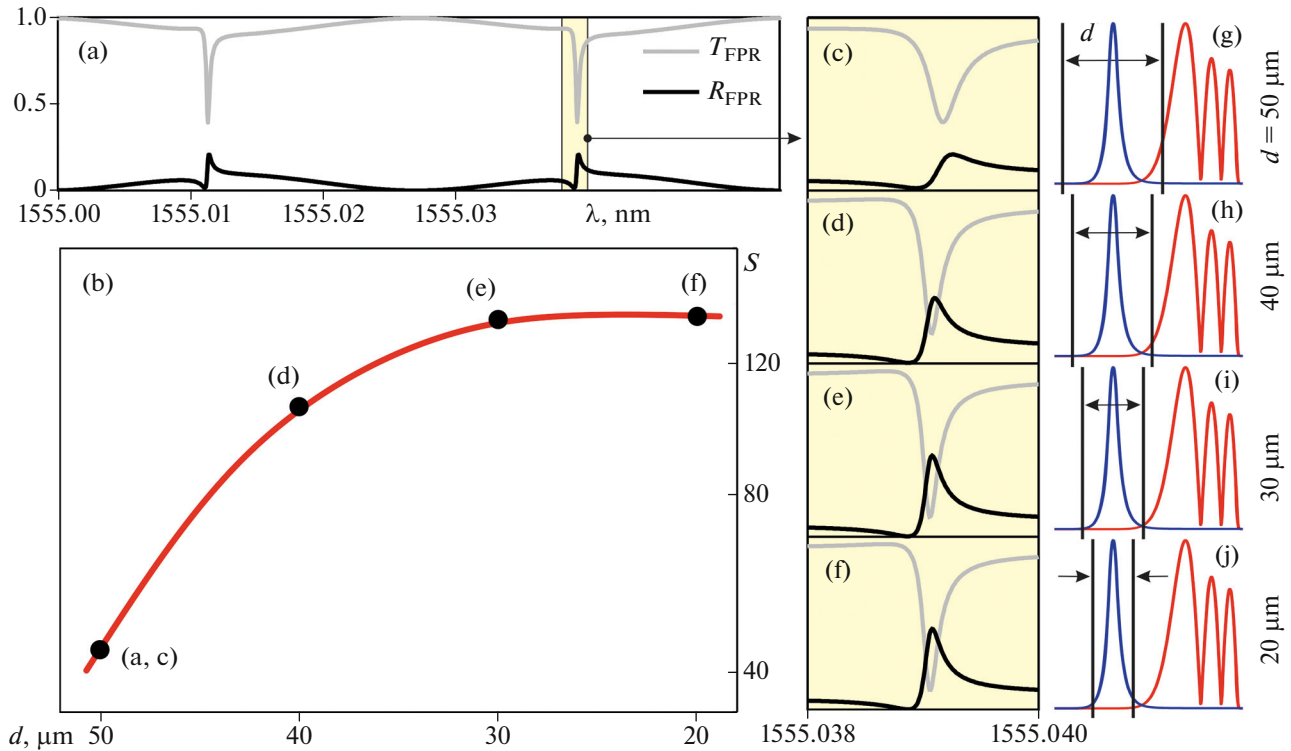


Fig. 5. Dependence of the Fano resonance sharpness S on the size of the hole in the metal mirrors (b). Reflection and transmission spectra of the BWR calculated at $d = 50 \mu\text{m}$, $R = 15.537 \text{ mm}$, $h_1 = h_2 = 100 \text{ nm}$, $L = 30 \text{ mm}$ (a); Insets (c–f) offer zoomed-in views of the resonance lineshapes at $d = 50 \mu\text{m}$ (c), $d = 40 \mu\text{m}$ (d), $d = 30 \mu\text{m}$ (e), and $d = 20 \mu\text{m}$ (f). Insets (g–j) show the boundaries of the hole in the mirror for various d values superposed on the amplitude profiles of the coupled FM and WGM.

however, are no longer associated with the transmission of light through the mirrors and can only be due to the diffraction and/or absorption of light in the mirrors. Throughout further calculations, we will use an excessively large mirror thickness of $h_2 = 100 \text{ nm}$ to eliminate the effect of transmission losses on the Q -factor of the WGM-subresonator.

The diffraction loss of the WGM-subresonator is determined by how strongly the WGM field is affected by the inner edge of the metal mirror. It depends on the size of the hole in the mirror d and on the width of the whispering gallery mode profile (Figs. 5g–5j). The width of WGM profile is larger for WGMs of higher orders (Figs. 1a–1c), therefore, at a fixed d , the diffraction losses of the WGM-subresonator will be more significant at smaller resonant bending radii where FM is coupled to WGMs of higher orders (see Fig. 1). By the same logic, for any chosen R_n , the diffraction loss should diminish, and the sharpness S should increase, with decreasing d (see Figs. 5g–5j). To confirm this conclusion, we plot at the below figure the dependence $S(d)$, as well as the reflection and transmission spectra of the BWR calculated at $d = 20, 30, 40,$ and $50 \mu\text{m}$, $R = R_3 = 15.537 \text{ mm}$.

As can be seen, the sharpness S does increase monotonically with decreasing the hole size, but this

trend is observed only if $d \gtrsim 30 \mu\text{m}$. At smaller d values, diffraction losses no longer affect the Q -factor of the WGM-subresonator, as illustrated by the visually indistinguishable resonance lineshapes at $d = 30 \mu\text{m}$ (Fig. 5e) and $20 \mu\text{m}$ (Fig. 5f). At $d \lesssim 20 \mu\text{m}$, the BWR spectra get distorted due to the edges of the mirror affecting the field of the fundamental mode. In further calculations, therefore, we set $d = 30 \mu\text{m}$ (at $R = 15.537 \text{ mm}$) to eliminate the effect of diffraction losses on the Q -factor of the WGM-subresonator, while also avoiding the spectral distortions.

The total radiation losses of the WGM-subresonator at $d = 30 \mu\text{m}$ and $h_2 = 100 \text{ nm}$ can thus be considered negligible, but even in their absence, the minimum in the resonant dip, as can be seen from Figs. 4f, 5e and 5f still does not reach 0. This suggests that the small but nonzero absorption losses in the metal mirrors do play a significant role in the BWR under study. The influence of the dissipative losses can be most clearly demonstrated while considering the dependence of the Fano resonance sharpness on the resonator length L .

The value of L affects the Q -factors of both coupled subresonators, which increase $\propto L$, as well as the free spectral range, which is included in the definition of the sharpness S . These circumstances make the dependence $S(L)$ somewhat more complicated than

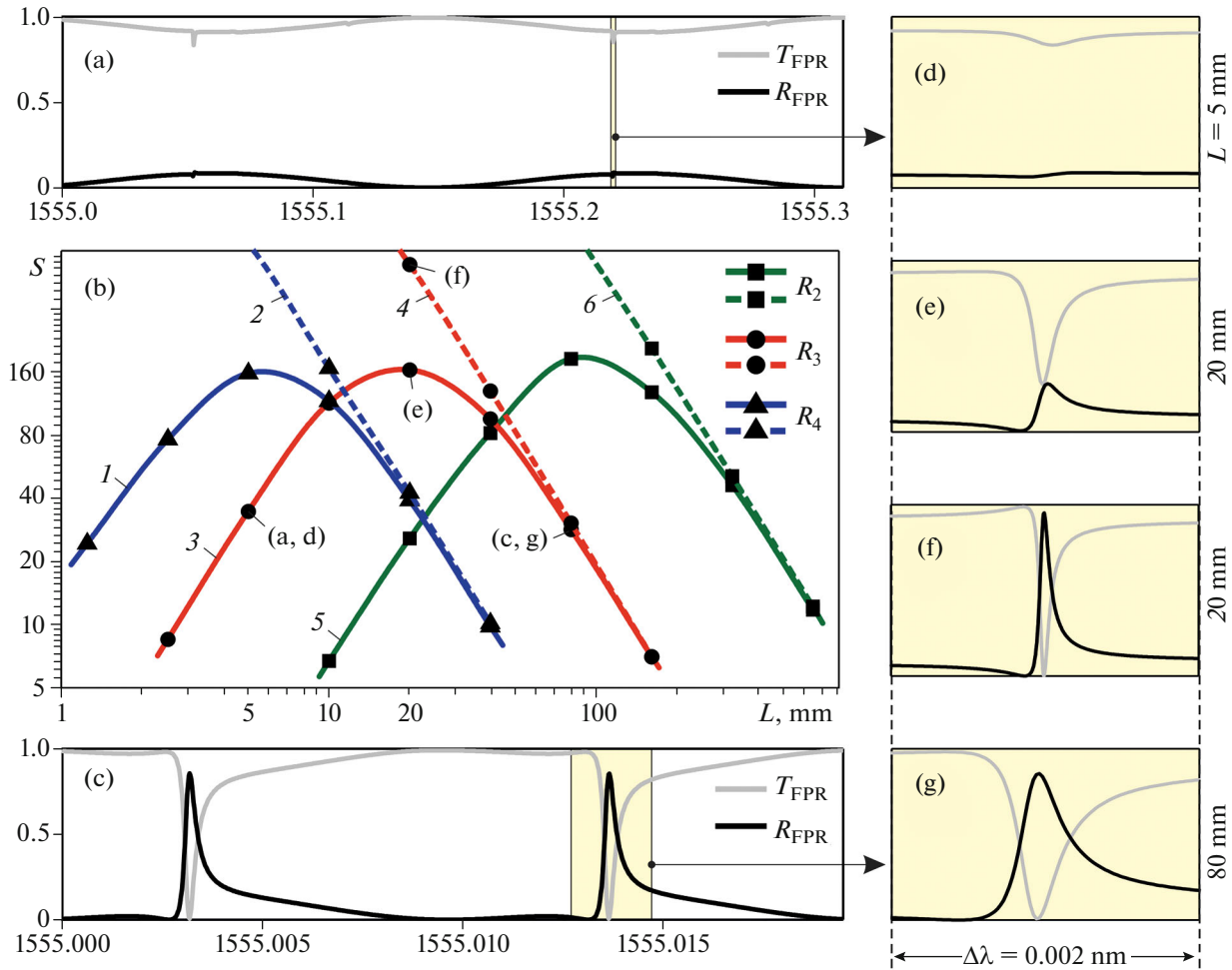


Fig. 6. Dependences of the Fano resonance sharpness S on the length of the resonator (b), calculated at $h_1 = h_2 = 100$ nm and $R = R_4 = 12.764$ mm, $d = 24$ μ m (1, 2), $R = R_3 = 15.537$ mm, $d = 30$ μ m (3, 4) and $R = R_2 = 19.269$ mm, $d = 34$ μ m (5, 6). Solid curves 1, 3, 5 were calculated for mirrors of ordinary silver, while dashed lines 2, 4, 6 were obtained for idealized lossless silver with the real-valued dielectric permittivity of $\tilde{\epsilon}_{Ag} = -130 + 0i$. Insets (a, c, d, e, g) show the reflection and transmission spectra of the BWR calculated with ordinary silver and $L = 5$ mm (a, d), $L = 20$ mm (e) and $L = 80$ mm (c, g). Inset (f) shows a zoomed-in view of the Fano lineshape obtained with the lossless silver and $L = 20$ mm.

the dependences $S(h_2)$ and $S(d)$ considered above. $S(L)$ calculated for three resonant bend radii, as well as the reflection and transmission spectra of the BWR at $L = 5, 20$ and 80 mm, $R = 15.537$ mm, are shown in Fig. 6.

Graphs 3 and 4 in Fig. 6b correspond to the dependence $S(L)$ calculated at $R = 15.537$ mm for two cases: with ordinary silver used as a mirror material (solid curve 3) and idealized silver with a real-valued permittivity $\tilde{\epsilon}_{Ag} = -130 + 0i$ (dashed line 4). In the second case, there are no dissipative losses in the mirrors, and the total losses of the WGM-subresonator can be considered zero. The depth of the resonant dip in this case reaches the maximum possible value of 100% at any L (as an example, Fig. 6f shows a zoomed-in view of the Fano lineshape at $L = 20$ μ m), and $S(L)$ can vary only

due to changes in the resonance width and the free spectral range of the BWR. Decreasing L leads to an increase in the free spectral range, while the width of the Fano resonance, as can be seen from the comparison of Figs. 6f and 6g, decreases. The latter trend is due to a decrease in the Q -factor of the FM-subresonator and is similar, in the mechanical system of coupled pendulums, to the narrowing of the resonant dip in the frequency response of the pendulum P1 with an increase in γ_1 at $\gamma_2 = 0, g \ll \gamma_1$. As a result of these two tendencies, as the resonator length decreases, the sharpness of the Fano resonances increases monotonically and without bound (dashed line 4 in Fig. 6b).

In the presence of dissipative losses of the WGM-subresonator, although the sharpness S does increase with decreasing the length of the BWR at large values of L , the growth is not without limit (solid curve 3 in

Fig. 6b): the sharpness reaches a maximum value of $S \approx 160$ at a certain optimal length $L_{\text{opt}} \approx 20$ mm, after which it decreases monotonically. This drop occurs due to a sharp decrease in the depth of the resonant dip (Figs. 6a, 6d), which is due to diminishing Q -factors of both WGM- and FM-subresonators and is similar to a decrease in the amplitude of the Fano resonance in the mechanical system with the growth of γ_2 and γ_1 at $0 < \gamma_2 \ll \gamma_1$ and $g \ll \gamma_1$.

The height of the local maximum in $S(L)$ will be the greater (and the value of L_{opt} the smaller), the closer to zero are the total losses of the WGM-subresonator. In our case, these losses are dissipative and cannot be further reduced. Moreover, in the chosen spectral range, silver, among all the widely available metals, has the smallest imaginary part of the permittivity and thus the minimum dissipative losses. A further reduction in the losses of the WGM-subresonator and corresponding enhancement of the sharpness of the Fano lineshapes are possible by using multilayer dielectric mirrors instead of metal ones. In practice, however, as the physical losses of the WGM-subresonator approach zero, it becomes necessary to consider the small but inevitable losses resulted from the technological limitations of its fabrication procedure. The maximum achievable sharpness of the resonant features in the BWR spectra, considering both physical and technological limitations, is thus the subject of a separate study.

Beside the Q -factors of the WGM- and FM-subresonators, whose influence has been being considered so far, the sharpness of the Fano resonances also depends on the FM-WGM coupling coefficient, which is smaller for larger resonant bend radii (Fig. 1f). To illustrate the effect of the bend radius, we have also plotted in Fig. 6b the dependences $S(L)$ calculated at $R = R_2 = 19.269$ mm (curves 5, 6) and $R_4 = 12.764$ mm (curves 1, 2). As can be seen, the weakening of the FM-WGM coupling with increasing R leads to a shift of $S(L)$ to the right. The maximum value of the sharpness, as well as the pattern of $S(L)$ for the cases of the real and lossless silver, remain practically unchanged. In the absence of dissipative losses (dashed lines 2, 4, 6), the sharpness S increases with R at any fixed value of L due to a narrower width of the resonance resulted from the weaker FM-WGM coupling. However, in the presence of absorption losses (solid curves 1, 3, 5), the weakening of FM-WGM coupling also brings about a sharp decrease in the depth of the resonant dip at small values of L . Combined together, these two trends lead to the shift of $S(L)$ to the right and a corresponding increase in the optimal resonator length, which amounts to $L_{\text{opt}} \approx 5$, 20 and 100 mm, respectively, for $R = 12.764$, 15.537 and 19.269 mm.

All the results presented above were obtained for the TE-polarized light in the waveguide. Calculations for the TM polarization yield similar results; however,

the resonant bend radii are slightly different due to the polarization dependence of WGM effective indexes.

CONCLUSIONS

Thus, tunable high- Q Fano resonances as well as spectral features characteristic of electromagnetically induced transparency have been demonstrated in the spectra of the bent waveguide-based Fabry–Perot resonator with variable reflectivity mirrors. The effect of the bend radius, mirror thickness, hole size, and resonator length on the position, shape, and sharpness of the narrow-band resonant features is investigated. It is shown that the maximum sharpness of the Fano lineshapes is $S \approx 160$, is limited by the dissipative losses of the WGM-subresonator, and is achieved at the optimal resonator length, which depends on its bend radius. It is shown that a further increase in the resonance sharpness can be achieved with lossless multilayer dielectric mirrors.

Due to the high sharpness and contrast of the demonstrated resonant features, the results obtained in the article can be used in the development of novel functional elements of photonics, especially bent waveguide-based sensing devices. Since the demonstrated effects arise from the coupling of the core mode with a cladding WGM, whose propagation constants depends on the bend radius, and whose field evanescently penetrates the external medium, they open exciting prospects for the development of novel high-performance portable refractometers for bio- and chemosensing applications, as well as optical sensors of mechanical effects. An additional advantage in this respect is the periodicity of the Fabry–Perot resonator spectra, which makes it possible to improve the measurement accuracy by averaging over many resonance lines.

Finally, we note that the effects studied in this work are demonstrated by the example of a simplified 2D geometry of a bent slab waveguide. In the 3D case of a bent fiber optic Fabry–Perot resonator, similar results should be expected. However, there will be much more Fano resonances in the reflection and transmission spectra of such a resonator since the cladding of a bent optical fiber supports many more whispering gallery modes. The results of the study of the three-dimensional case will be presented in a subsequent publication.

FUNDING

The presented study was supported by the Russian Foundation for Basic Research (grant no. 20-02-00556A).

CONFLICT OF INTEREST

The authors declare that they have no conflicts of interest.

REFERENCES

1. Fano, U., *Phys. Rev.*, 1961, vol. 124, no. 6, p. 1866.
2. Limonov, M.F., Rybin, M.V., Poddubny, A.N., et al., *Nat. Photonics*, 2017, vol. 11, no. 9, p. 543.
3. Garrido Alzar, C.L., Martinez, M.A.G., and Nussenzeveig, P., *Am. J. Phys.*, 2002, vol. 70, no. 1, p. 37.
4. Fan, S., Suh, W., and Joannopoulos, J.D., *J. Opt. Soc. Am. A*, 2003, vol. 20, no. 3, p. 569.
5. Wang, F., Wang, X., Zhou, H., et al., *Opt. Express*, 2009, vol. 17, no. 9, p. 7708.
6. Luk'yanchuk, B., Zheludev, N.I., Maier, S.A., et al., *Nat. Mater.*, 2010, vol. 9, no. 9, p. 707.
7. Chong, K.E., Hopkins, B., Staude, I., et al., *Small*, 2014, vol. 10, no. 10, p. 1985.
8. Kuznetsov, A.I., Miroshnichenko, A.E., Brongersma, M.L., et al., *Science*, 2016, vol. 354, no. 6314, aag2472.
9. Miroshnichenko, A.E., Flach, S., and Kivshar, Y.S., *Rev. Mod. Phys.*, 2010, vol. 82, no. 3, p. 2257.
10. Rahmani, M., Luk'yanchuk, B., and Hong, M., *Laser Photonics Rev.*, 2013, vol. 7, no. 3, p. 329.
11. Yu, Y., Xue, W., Semenova, E., et al., *Nat. Photonics*, 2017, vol. 11, no. 2, p. 81.
12. Lu, H., Liu, X., Mao, D., et al., *Opt. Lett.*, 2012, vol. 37, no. 18, p. 3780.
13. Zhang, S., Bao, K., Halas, N.J., et al., *Nano Lett.*, 2011, vol. 11, no. 4, p. 1657.
14. Cetin, A.E. and Altug, H., *ACS Nano*, 2012, vol. 6, no. 11, p. 9989.
15. Wu, C., Khanikaev, A.B., Adato, R., et al., *Nat. Mater.*, 2012, vol. 11, no. 1, p. 69.
16. Singh, R., Cao, W., Al-Naib, I., et al., *Appl. Phys. Lett.*, 2014, vol. 105, no. 17, 171101.
17. Dyshlyuk, A.V., *Opt. Lett.*, 2019, vol. 44, no. 2, p. 231.
18. Dyshlyuk, A.V., Eryusheva, U.A., and Vitrik, O.B., *J. Lightwave Technol.*, 2020, vol. 38, no. 24, p. 6918.
19. Novotny, L., *Am. J. Phys.*, 2010, vol. 78, no. 11, p. 1199.
20. Snyder, A.W. and Love, J., *Optical Waveguide Theory*, Berlin: Springer, 2012.
21. Johnson, P.B. and Christy, R.W., *Phys. Rev. B*, 1972, vol. 6, no. 12, p. 4370.
22. Dyshlyuk, A.V., Vitrik, O.B., Kulchin, Yu.N., et al., *J. Lightwave Technol.*, 2017, vol. 35, no. 24, p. 5425.
23. Wang, P., Semenova, Yu., Wu, Q., et al., *Appl. Opt.*, 2009, vol. 48, no. 31, p. 6044.
24. Wang, P., Semenova, Yu., Li, Y., et al., *Photonics Lett. Pol.*, 2010, vol. 2, no. 2, p. 67.
25. Kulchin, Y.N., Vitrik, O.B., and Gurbatov, S.O., *Quantum Electron.*, 2011, vol. 41, no. 9, p. 821.
26. Homola, J., *Surface Plasmon Resonance Based Sensors*, Heidelberg: Springer, 2006.